Halide-exchanged perovskite photodetectors for wearable visible-blind ultraviolet monitoring

Yu Zhou [a,c,1], Xiao Qiu [a,c,1], Zhu'an Wan [a,1], Zhenghao Long [a,c], Swapnadeep Poddar [a], Qianpeng Zhang [a,c], Yucheng Ding [a,c], Chak Lam Jonathan Chan [a], Daquan Zhang [a,c], Kemeng Zhou [d], Yuanjing Lin [d], Zhiyong Fan [a,b,c,*]

[a] *Department of Electronic & Computer Engineering, The Hong Kong University of Science and Technology, Clear Water Bay, Kowloon, Hong Kong, China*
[b] *Department of Chemical and Biological Engineering, The Hong Kong University of Science and Technology, Clear Water Bay, Kowloon, Hong Kong, China*
[c] *Guangdong-Hong Kong-Macao Joint Laboratory for Intelligent Micro-Nano Optoelectronic Technology, The Hong Kong University of Science and Technology, Hong Kong, China*
[d] *School of Microelectronics, Southern University of Science and Technology, Shenzhen, China*

ARTICLE INFO

ABSTRACT

Wearable sensing technologies are essential for personalized healthcare via continuously monitoring the surrounding information. Ultraviolet (UV) light, an important component of solar radiation, is recognized as the main inducement of skin cancers. So far, the use of rigid and costly technologies to fabricate UV sensors still hinders their implementation in wearable and portable electronics. Here we present a wearable UV wristband based on a self-powered flexible perovskite photodetector for real-time UV monitoring. Utilizing a solution-assisted halide exchange strategy, device based on $CH_3NH_3PbCl_3$ film exhibits excellent UV detection performance (high responsivity of 359.03 mA/W, fast rise/fall time of 3.91/4.55 ms), outstanding mechanical robustness (remaining over 80% of initial performance after 2500 bending cycles), as well as desirable operational stability (unchanged photoresponse under 500 h of continuous UV light soaking). Integrated with commercially available soft circuits, this fully flexible sensor system enables round-the-clock probing for UV radiation indoor and outdoor in conjunction with necessary environmental information, which can be displayed and recorded on a smartphone, to prevent prolonged UV exposure. The wearable platform not only paves the way for seamlessly integrated photodetectors, but also enables a wide range of personalized environmental and health monitoring applications.

1. Introduction

Sunlight is the primary source of light and heat for living beings. Current evidence indicates ultraviolet (UV) radiation from daily sunlight plays an instrumental role in vitamin D synthesis within the human body [1,2]. However, excessive UV exposure is a proven precipitating factor for sunburn, skin aging, and skin cancer, which is the most common cancer worldwide [3–6]. The UV spectrum covers the wavelength range from 100 to 400 nm and can be classified into UVA, UVB, and UVC, which correspond to wavelength intervals of 315–400 nm, 280–315 nm, and 100–280 nm, respectively [7,8]. All UVC and ca. 90% of UVB radiation are absorbed when they pass through the atmosphere [9,10].

Therefore, wearable UV sensors with real-time and accurate detection for the UV radiation composed of UVA with a small portion of UVB are highly desired to protect us from the potential risk of prolonged UV exposure.

Recent advances in materials and optoelectronics have enabled the rapid development of UV sensors. According to the working mechanism, they can be divided into photochemical materials and photoelectric materials-based sensors [11]. For example, Lee et al. reported a photo-cleavable polymer-based UV sensor, which could transform from transparent to yellow under continuous UV exposure [12]. Shi et al. developed a soft UV patch with photosensitive patterned dye, which exhibited different color patterns corresponding to UV light intensity

[13]. Employing the colorimetric concept, photosensitive materials-based UV sensors are feasible for portable and wearable UV dosimeter. However, they can hardly provide real-time UV analysis or accurate spectrum response. In contrast, UV photodetectors (PDs) based on conventional inorganic photoelectric semiconductors, such as AlGaN [14,15], GaN [16], SiC [17], Ga_2O_3 [18] and other metal oxides [19–21], often exhibit high responsivity under external bias, while suffering from relatively slow response time (>1 s) and poor zero-bias photoresponsivity (< 10 mA/W). Compatibilities between high-quality inorganic films and soft substrate as well as high-cost manufacturing pose significant challenges for their further utilization in wearable UV sensors.

Emerging halide perovskites with tunable band gap, long carrier diffusion length, and high absorption coefficient have attracted tremendous attention over the past decade, exhibiting great potential in optoelectronic fields [22–27]. In this regard, excellent spectrum selectivity renders perovskites as promising candidates for photodetection [28,29]. Among lead halide perovskites, lead chloride perovskites exhibit the widest band gap. As a family member of lead chloride perovskites, methylammonium lead chloride ($MAPbCl_3$) has a wider band gap compared with formamidinium lead chloride ($FAPbCl_3$) and cesium lead chloride ($CsPbCl_3$), which makes it particularly suitable in UV sensing applications [30–33]. Moreover, $MAPbCl_3$ is thermally stable and can maintain the cubic phase from ca. −95–200 °C [34]. However, solution-processed chloride perovskite usually demonstrates poor film morphology and crystallinity with undesirable pinholes and cracks, due to its lower formation energy and decomposition temperature, compared with iodide and bromide counterparts, thus limiting the device performance [35,36]. Herein, we propose a facile solution-assisted halide exchanged (SAHE) $MAPbCl_3$ film-based UV photodetector with high responsivity and fast response time without external bias. Compared with the conventional solution process, $MAPbCl_3$ film based on the SAHE method shows better film morphology and enhanced crystallinity. As a result, flexible UV PDs demonstrate impressive mechanical robustness and multi-environmental operational stability. Merging flexible sensors with commercially available integrated circuit technology and flexible printed circuit board (FPCB), we develop a wearable flexible UV wristband with functions of sensing, signal processing, and wireless communication, which can provide real-time UV monitoring in various conditions.

2. Result and discussion

A facile halide exchange technique was utilized to convert the uniform conventional solution processed $MAPbBr_3$ ($MAPbBr_3$-CS) film into $MAPbCl_3$ film, as illustrated in Fig. 1a. Specifically, dense $MAPbBr_3$ was first fabricated by the conventional solution process. After that, $MAPbBr_3$ was immersed in saturated MACl solution for halide exchange. Fig. 1b describes the mechanism for the element diffusion and exchange. During this process, Br elements in $MAPbBr_3$ were gradually replaced by Cl elements with the increased immersion time, which was evidenced by the gradual blue shift of absorption edge and right shift of typical (100) diffraction peak, extracted from the ultraviolet-visible (UV–vis) absorption and X-ray diffraction (XRD) spectroscopy (Fig. S1), respectively. As a result, $MAPbBr_3$ shrunk along grain boundaries and was totally transformed into $MAPbCl_3$ after halide exchange for 30 min. Compared with conventional solution-processed $MAPbCl_3$ ($MAPbCl_3$-CS) film with massive pinholes and disordered crystallinity, $MAPbCl_3$ fabricated by SAHE method ($MAPbCl_3$-SAHE) exhibited much improved film morphology and well-aligned grains (Figs. 1c and S2). It is noted that cracks induced by the crystal shrinkage during halide exchange mainly distribute near the $MAPbCl_3$-SAHE film surface rather than the bottom due to the adhesion and confinement of substrate. To further confirm the total halide replacement in perovskites, we checked the XRD, UV–vis absorption, and X-ray photoelectron spectroscopy (XPS) results of three different films. In Fig. 1d, the diffraction peaks at 15.1° and 30.2° are ascribed to (100) and (200) facets of $MAPbBr_3$ cubic phase, and shifted to 15.6° and 31.5°, respectively, fitting well with corresponding facets of $MAPbCl_3$-CS here and $MAPbCl_3$ cubic phase as reported before [35,37]. The right shift of diffraction peaks and ordered peak shape verified the complete conversion from $MAPbBr_3$ to $MAPbCl_3$ as well as the superior crystallinity of $MAPbCl_3$-SAHE to that of $MAPbCl_3$-CS. According to the XPS result in Fig. S3, no Br signal can be observed from the Br 3d spectra of $MAPbCl_3$-SAHE film, and the typical XPS spectra of $MAPbCl_3$-SAHE correspond well with those of $MAPbCl_3$-CS. Meanwhile, the obvious change of band gaps extracted
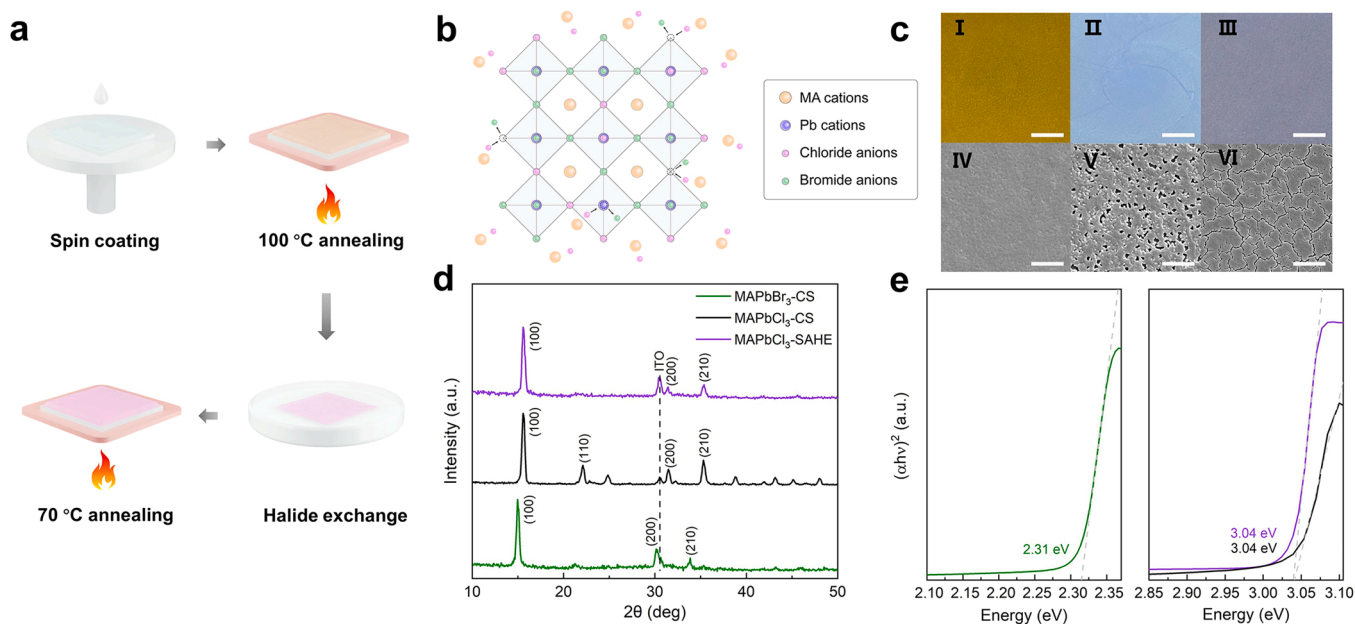

Fig. 1. Solution-assisted halide exchange (SAHE) method for $MAPbCl_3$ deposition. (a) Schematic diagram of the SAHE method and (b) exchange mechanism in the perovskite film. (c) Photograph and SEM images of $MAPbBr_3$-CS (I, IV) and $MAPbCl_3$-CS (II, V) and $MAPbCl_3$-SAHE (III, VI), respectively. Scale bar, 2 mm for I to III, 2 μm for IV to VI. d) XRD spectra. e) Tauc plot for estimating the direct band gap of $MAPbBr_3$-CS (green line), $MAPbCl_3$-CS (black line), and $MAPbCl_3$-SAHE (violet line).

from the tauc plot in Fig. 1e, 2.31 eV for MAPbBr$_3$-CS, 3.04 eV for MAPbCl$_3$-CS and MAPbCl$_3$-SAHE, respectively, was in congruence with the photoluminescence (PL) emission peak positions (Fig. S4a). Photo-electron spectroscopy in the air (PESA) measurement was carried out to estimate the valence band maximum (VBM) of MAPbBr$_3$-CS and MAPbCl$_3$-SAHE to be −5.56 and −5.84 eV (Fig. S4b), thereby providing clinching evidence for complete chloride substitution.

Based on uniform MAPbCl$_3$-SAHE films, we constructed rigid UV PD with the vertical configuration of Glass/ITO/SnO$_2$/MAPbCl$_3$/PTAA/Au as illustrated in Figs. 2a and S5, in which SnO$_2$ acts as electron transporting layer and PTAA serves as hole transporting layer. As shown in Fig. 2b, suitable energy level alignment between MAPbCl$_3$ and adjacent charge transporting layers enables UV PD to be self-powered and work in photodiode mode. To compare the PD performance of MAPbCl$_3$-SAHE with that of MAPbCl$_3$-CS, time-domain response under 395 nm light with the intensity of 0.494 mW/cm^2 and corresponding dark current of
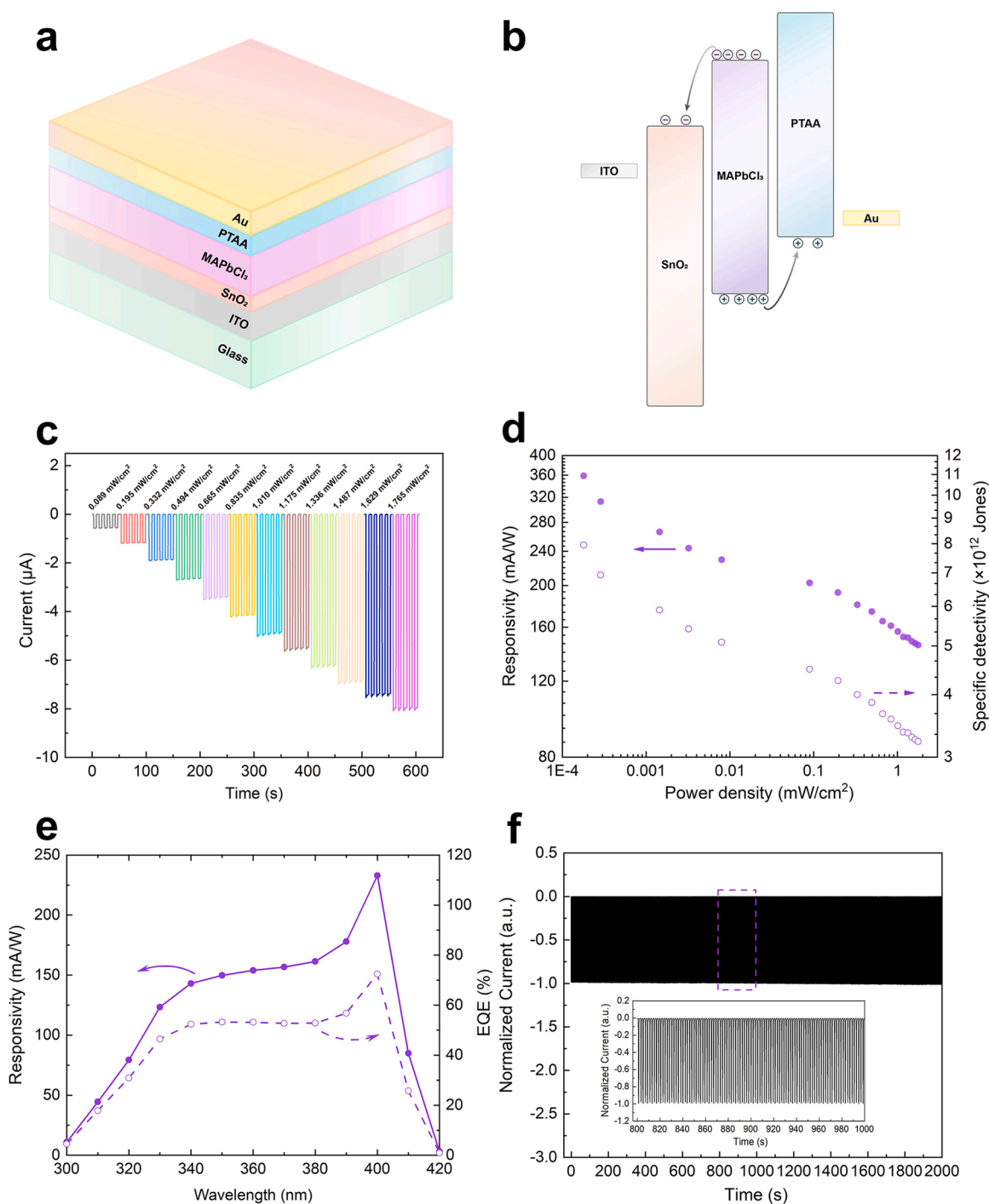

Fig. 2. Photoresponse characteristics of the MAPbCl$_3$-SAHE UV photodetector on rigid substrate. (a) Schematic illustration of the rigid device structure. (b) Energy level alignment of UV photodetector, showing the photogenerated carrier transfer after UV illumination. (c) Time-domain response. (d) Responsivity and specific detectivity of the rigid photodetector as a function of incident intensity under 395 nm light illumination. (e) Responsivity and EQE of the rigid device as a function of wavelength with the light intensity of 0.494 mW/cm^2. (f) Time-dependent on/off switching behavior of rigid photodetector under 395 nm light source with the intensity of 0.494 mW/cm^2. Inset, zoom-in image from 800 to 1000 s. All the tests were performed on unencapsulated devices in ambient environment (at ~23–28 °C and ~45–55% relative humidity), unless otherwise specified.

the rigid devices were tested (Fig. S6). The statistics result indicated that PDs based on MAPbCl$_3$-SAHE exhibited better photoresponse and smaller dark current (201 $\pm$ 6 pA) than those of PDs based on MAPbCl$_3$-CS, together with good reproducibility. Semilogarithmic current–voltage (I-V) curve of the device under dark and illumination of 395 nm light with the intensity of 0.494 mW/cm^2 (Fig. S7a) further verified the rectifying characteristics and remarkable photocurrent of PD based on MAPbCl$_3$-SAHE. Fig. 2c demonstrates the time-domain response of the rigid device under different 395 nm light intensities. As the light intensity changed from 0.18 μW/cm^2 to 1.765 mW/cm^2, photocurrent increased gradually with high consistency (Fig. S7b). To assess the performance of UV PD based on MAPbCl$_3$-SAHE film, the critical figure-of-merit parameters, including responsivity (R_λ), specific detectivity (D^*), external quantum efficiency (EQE) have been evaluated, which can be defined by the following equations, respectively.

$$R_\lambda = \frac{J_{light} - J_{dark}}{P_{in}} \quad (1)$$

$$D^* = \frac{R_\lambda}{\sqrt{2eJ_{dark}}} \quad (2)$$

$$EQE = \frac{R_\lambda hc}{e\lambda} \quad (3)$$

Specifically, R_λ represents the device response to the incident light under certain wavelength, in which J_{light}, J_{dark}, P_{in}, and λ are the photocurrent density, dark current density, incident light intensity, and excitation wavelength. D^* reflects the weakest light that the device can detect, which can be simplified as abovementioned since the shot noise mainly contributes to the dark current at room temperature [23,38,39]. EQE describes the conversion efficiency from photons to electrons,

where h, c, and e are the Planck's constant, light speed, and elementary charge, respectively. A maximum R_λ of 359.03 mA/W was obtained at 0 V under 395 nm light illumination with the intensity of 0.18 μW/cm^2, as shown in Fig. 2d. Owing to the low dark current in the n-i-p device structure, the corresponding D^* reached up to 7.95 $\times$ 10^{12} Jones. As the light intensity increases, R_λ shows a descending trend, which is attributed to the fitted relationship of $I \propto P_{in}^{0.93}$ between photogenerated current and incident light intensity (Fig. S7b). Plotting R_λ and EQE versus light wavelength, we identified the cut-off response wavelength of 420 nm. Since R_λ declined rapidly over the wavelength of 400 nm, UV detector exhibited visible-blind property. To explore the photoresponse dynamic stability, time-dependent on/off switching behavior was tracked under 395 nm light (0.494 mW/cm^2) for over 2000 s. The unchanged current after thousands of switching cycles implied the outstanding operational stability of UV PDs. The response time (rise time/fall time) of UV PD under 395 nm light with the intensity of 0.494 mW/cm^2 calculated from the transient photoresponse test (Fig. S7c) were 3.91 and 4.55 ms, respectively. It is worth mentioning that UV PD based on MAPbCl$_3$-SAHE film exhibited competitive detection performance compared with those based on MAPbCl$_3$ with other fabrication processes or based on other perovskite materials, as summarized in Table S1.

The low-temperature process of MAPbCl$_3$-SAHE enables its feasibility for flexible UV PDs. To further verify the properties of MAPbCl$_3$-SAHE in flexible devices, related photoresponse performance was characterized by replacing ITO glass with ITO/PET substrate. As illustrated in Figs. 3a and b, flexible UV PD based on MAPbCl$_3$-SAHE presented clear and continuous interface, which did promote the interface contact and enhance the charge transfer. Similar to the rigid device, flexible UV PD exhibited well-consistent photoresponse with increased incident light intensity (Fig. 3c), thus achieving a champion R_λ of
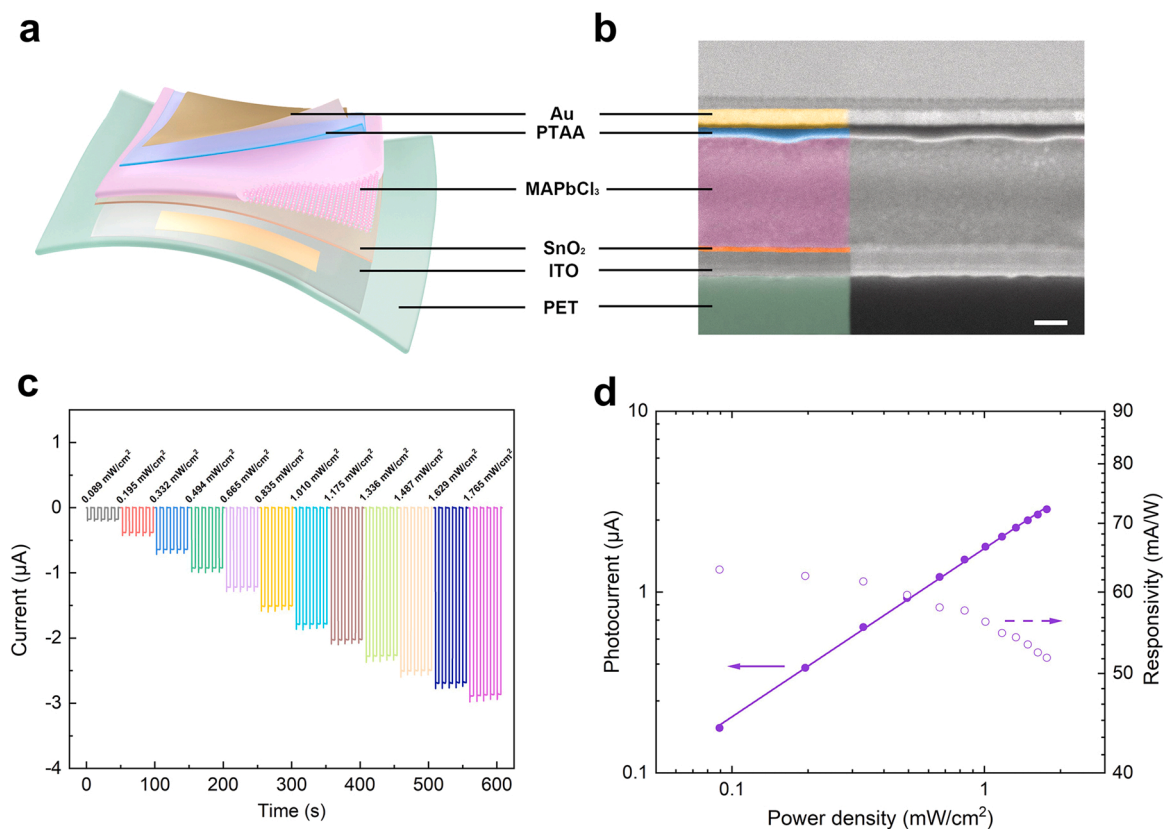

Fig. 3. Photoresponse characteristics of flexible MAPbCl$_3$-SAHE UV photodetector. (a) Schematic illustration of flexible device architecture. (b) Cross-section SEM image of the flexible device. Scale bar, 100 nm. (c) Time-domain response. (d) Photocurrent and responsivity of the flexible photodetector as a function of incident intensity under 395 nm light source. All the tests were performed on unencapsulated devices in ambient environment (at ~23–28 °C and ~45–55% relative humidity), unless otherwise specified.

63.08 mA/W at 395 nm light illumination with the intensity of 0.089 mW/cm². As plotted in Fig. 3d, with the enhanced UV light intensity, photocurrent of flexible UV PD increased continuously following the same formula of $I \propto P_{in}^{0.93}$ to that of the rigid device, which further evidenced the outstanding consistency and reproductivity of both rigid and flexible UV PDs. Considering the poorer transparency of ITO/PET than those of ITO glass in the UV wavelength range, it is promising to further improve the performance of flexible UV PD by employing better substrates. Noted that our UV PDs on rigid and flexible substrates already showed superior performance compared with other types of self-powered UV-PDs (Table S2).

To evaluate the multi-robustness of flexible UV PDs for promising applications in wearable UV sensors, we inspected the stability of flexible UV PDs from various aspects. Fig. 4a depicts the mechanical stability of flexible devices under different bending radius for 50 cycles by attaching the device onto cylinders. When the bending radius reduced to less than 4 mm, flexible UV PD retained less than 90% of its original photoresponsivity, implying the slight mechanical damage of the ITO/PET substrate. It is noted that the flexible device remained over 70% of its initial photoresponse even under the bending radius of 1 mm. As displayed in Fig. 4b, the bending robustness of the flexible device was further investigated during sequential 5000 bending cycles with a fixed bending radius of 7 mm. Surprisingly, photoresponsivity of flexible UV PD retained more than 81% of its initial value even after 2500 cycles, which plummeted to 73% when the number of cycles reached up to 5000. We directly tracked the perovskite and device surface morphologies by optical microscope (Fig. S8) during the bending process. The cracks in the film formed and enlarged with the increased bending cycles, thus causing the performance degradation, which well agreed with

previously reported works [40,41]. Assuming the resistance of ITO/PET substrate remained unchanged under 7 mm bending radius, the high film quality of MAPbCl₃-SAHE as well as the solid interface between perovskite and neighboring layers simultaneously contributed to the decent mechanical robustness [42,43]. Besides, the aging properties of flexible UV PDs under continuous light soaking and after storage in dry box were monitored. As exhibited in Fig. 4c, the flexible device encapsulated by polydimethylsiloxane (PDMS) kept steady current during 500-hour continuous 395 nm UV light soaking. Meanwhile, the unencapsulated device stored in dry box retained 96% of its primary value after 30 days (Fig. 4d). The above findings indicated the excellent multi-robustness of flexible UV PDs under different operation conditions.

The flexible UV PDs with respectable detection performance and great operational stability suggested that they have a promising potential for wearable real-time UV sensor. Integrated flexible UV PD with commercial FPCB, we demonstrated a practical wearable UV monitoring wristband as illustrated in Figs. 5a and b. Noted that our UV PD was well encapsulated by PDMS after soldered onto FPCB, thus Pb leakage and potential hazards to users could be effectively prevented [44–46]. We further estimated the Pb content in the integrated flexible UV PD as shown in the Table S3. The Pb content inside is calculated to be 37.2 ppm, which is far below the EU RoHS regulation limit of 1000 ppm. Once the flexible UV PD senses the UV light, the sensing signal will be transmitted to the integrated-circuit components, which can provide effective functionalities of signal conditioning, processing, and wireless communication. Finally, real-time UV radiation data can be displayed on users' interfaces and further uploaded to cloud servers (Fig. S9a). In addition, temperature and relative humidity sensors were installed on
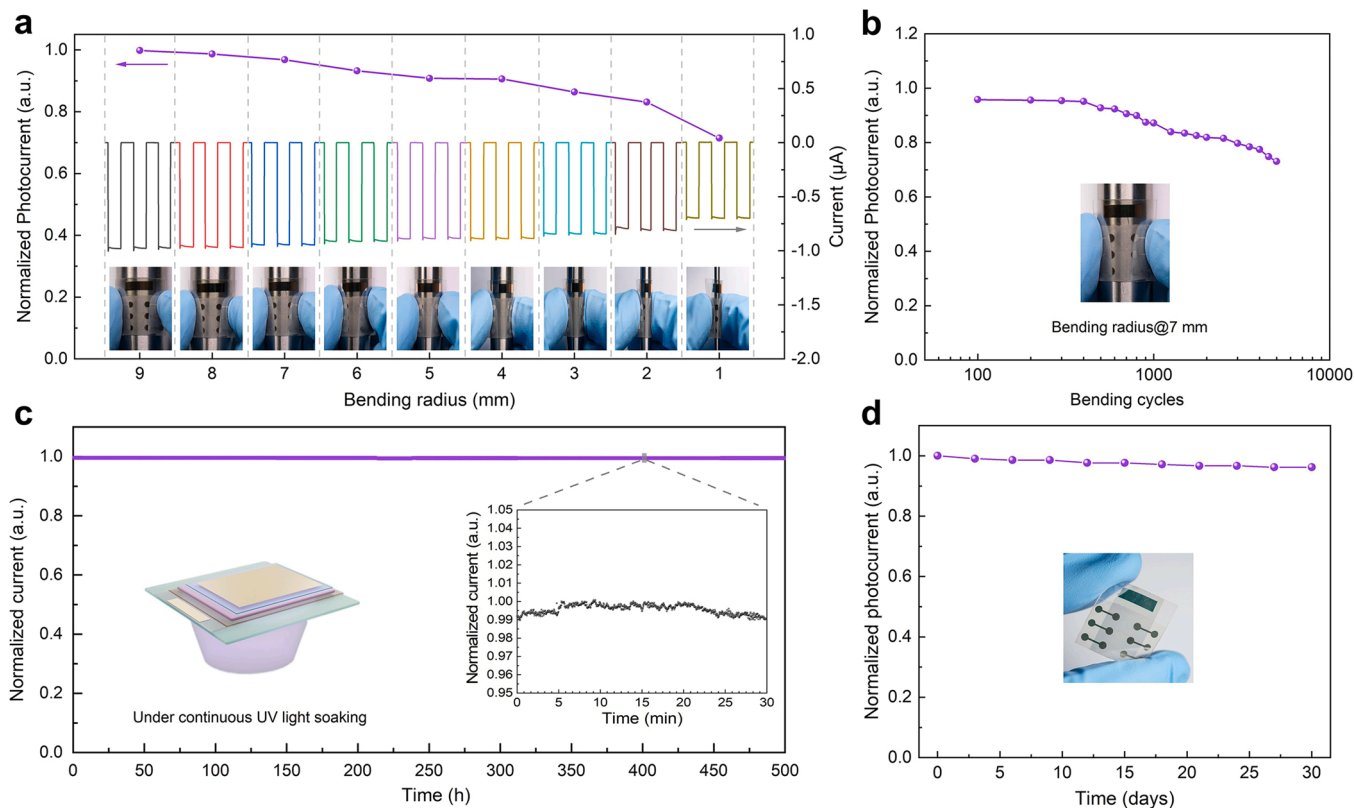

Fig. 4. Multi-stability characteristics of flexible MAPbCl₃ UV photodetector. (a) Bending stability for 50 cycles with different bending radius. Insets, photographs of unencapsulated flexible devices with different bending radius. (b) Bending stability for different cycles with a fixed bending radius of 7 mm. Inset, photograph of corresponding unencapsulated device. (c) Aging test of the encapsulated device under continuous light soaking in the ambient environment. Insets, schematic diagram of aging test and zoom-in image from 400 to 400.5 h. (d) Storage stability in dry box. Inset, photograph of the tested unencapsulated device. All these data were collected under 395 nm light source with the intensity of 0.494 mW/cm² and all the tests were performed in ambient environment (at ~23–28 °C and ~45–55% relative humidity), unless otherwise specified.
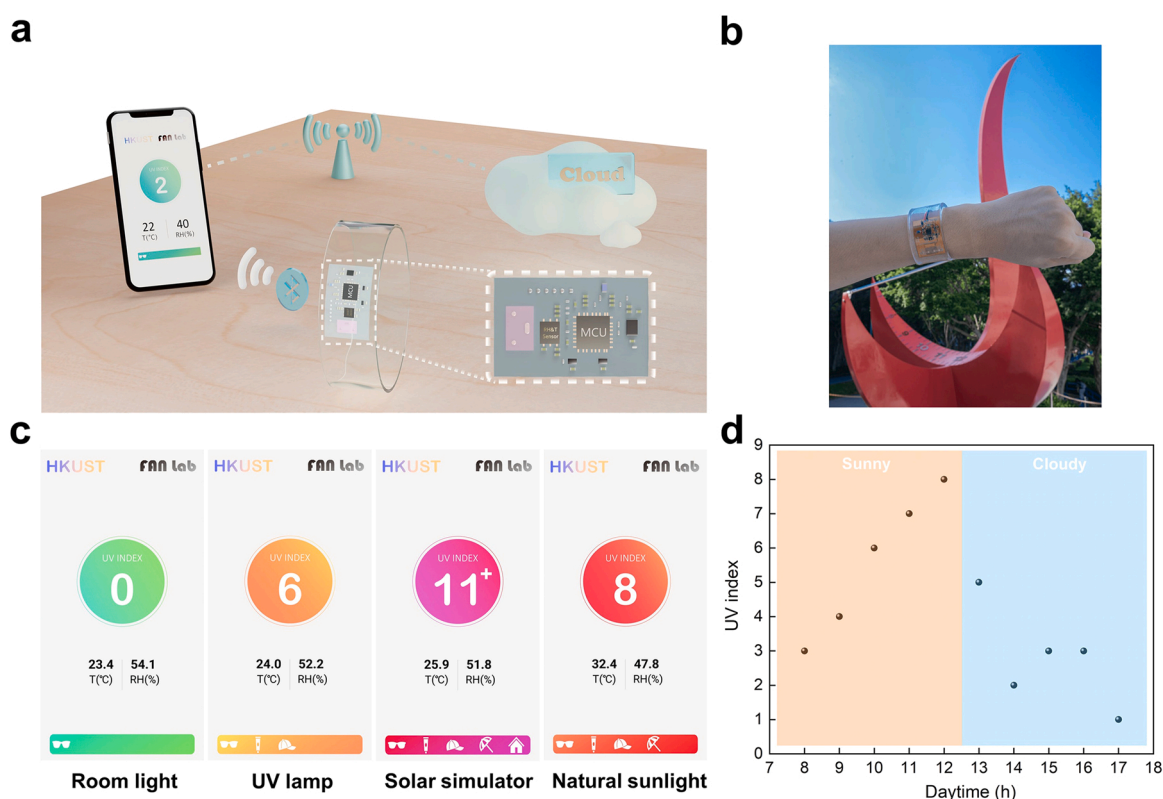
Fig. 5. Wearable UV monitoring wristband. (a) Schematic illustration showing the UV monitor works in daily life. The data can be transmitted to the user's mobile phone and uploaded to the cloud. (b) Photograph of a wearable flexible UV monitor. (c) UV index measured by flexible UV monitor under different light sources. (d) Round-the-clock UV monitoring by the wearable wristband.

the wristband to facilitate valid evaluation of real-time UV radiation indoor and outdoor, as illustrated in the system-level block diagram (Fig. S9b). To verify the working aptitude of wearable UV wristband, it was employed to monitor real-time UV radiation under different kinds of light sources as demonstrated in Fig. 5c, e.g., room light, UV lamp, solar simulator, and natural sunlight, respectively. Through wireless communication, we can conveniently read and save all these data on the phone (Video S1). Besides, real-time UV radiation monitoring by UV wristband was performed on a subject outdoor during the whole daytime as shown in Fig. 5d, which recorded the real-time UV radiation variation and duration time. The changing trend agreed well with the data recorded by the Hong Kong Observatory. Moreover, our fully flexible UV monitor can be easily integrated into various wearable and smart scenarios, such as cap, clothes, umbrella, and quadrupedal robot (Fig. S10), which could be adaptive to different requirements of users. These results indicated that our perovskite UV monitor could effectively provide real-time UV exposure data, environmental information (temperature, relative humidity) together with reasonable suggestions to thwart users from the risk of excessive UV exposure.

Supplementary material related to this article can be found online at doi:10.1016/j.nanoen.2022.107516.

3. Conclusion

In summary, we utilized a facile solution-assisted halide exchange method to fabricate rigid and flexible UV photodetectors based on high-quality $MAPbCl_3$ films. UV PDs based $MAPbCl_3$-SAHE films exhibited excellent photoresponsivity (359.03 mA/W), respectable specific detectivity (7.95×10^{12} Jones), and fast response time of rise and fall (3.91 and 4.55 ms) under self-powered operation mode. Owing to the high film morphological quality and crystallinity, flexible UV PDs exhibited impressive mechanical robustness and operational stability.

Merging flexible UV sensors with commercially available integrated circuits on a home built FPCB, we realized a wearable UV wristband for real-time UV radiation monitoring indoor and outdoor. The fully flexible system can be expediently integrated with other portable and wearable sensors for all-round real-time environment parameter monitoring.

4. Experimental section

4.1. Materials

Methylammonium bromide (MABr, 99.99%), methylammonium chloride (MACl, 99%) were purchased from Greatcell Solar Materials. Lead bromide ($PbBr_2$, 99.999%, trace metals basis), lead chloride (99.999%, trace metals basis), dimethyl sulfoxide (DMSO, anhydrous, 99.9%), dimethylformamide (DMF, anhydrous, 99.8%), isopropanol (IPA, anhydrous, 99.5%) were bought from Sigma Aldrich. Tin (IV) oxide nanoparticles (15% in H_2O colloidal dispersion) and chlorobenzene (Spectrophotometric Grade, 99.9%) were purchased from Alfa Aesar. Poly(triarylamine) (PTAA, M_n = 15000–25000) was purchased from Xi'an Polymer Light Technology Corp. Polydimethylsiloxane (PDMS) and Sylgard-184 were purchased from Dow Corning. Indium tin oxide (ITO) coated glasses (7–9 Ω/sq) and ITO coated polyethylene terephthalate (ITO/PET, 8–10 Ω /sq) were purchased from Advanced Election Technology Co., Ltd. All the materials were used as received without any further purification.

4.2. Precursor preparation

SnO_2 precursor solution was prepared by diluting 600 μL SnO_2 colloidal dispersion in 3 mL H_2O and stirred for 5 h. $MAPbBr_3$ perovskite precursor solution was prepared by dissolving MABr (1.0 M) and $PbBr_2$ (1.0 M) in anhydrous DMF/DMSO (1/1, v/v) mixture. $MAPbCl_3$

perovskite precursor solution was prepared by dissolving MACl (1.0 M) and $PbCl_2$ (1.0 M) in anhydrous DMF/DMSO (1/1, v/v) mixture. The perovskite precursor solutions were stirred overnight and filtered with a 0.22 μm PTFE-filter before use. MACl solution was prepared by dissolving in IPA with the concentration of 7 mg/mL. The PTAA solution was prepared by dissolving in chlorobenzene with the concentration of 20 mg/mL. Polydimethylsiloxane (PDMS) and Sylgard-184 were mixed with the weight ratio of 10:1, then the PDMS mixture was stirred for 5 min and pumped for 20 min to eliminate air bubbles.

4.3. Device fabrication

Patterned ITO-coated glasses were cleaned in sequence with detergent, deionized water, ethanol, acetone, and IPA. Patterned ITO/PET substrates were cleaned with detergent, deionized water, ethanol, and IPA. Before use, ITO-coated substrates were blown to dry by N_2 and exposed to O_2 plasma for 15 min. The SnO_2 precursor solution was spin-coated at 4000 rpm for 30 s. The substrate was then heated at 125 °C for 40 min and cooled down slowly to room temperature on a hot plate. For the conventional solution process, perovskite precursor solutions were spin-coated on the substrate (2000 rpm for 10 s, then 5000 rpm for 20 s) with quick drop of 150 μL chlorobenzene at 5 s before the end of the second spinning process. The intermediate film was then annealed at 100 °C for 20 min. For the solution-assisted halide exchange process, the fresh $MAPbBr_3$ film was immersed into as-prepared MACl solution at room temperature in the glovebox for different time periods, then rinsed with IPA three times. The as-prepared film was further dried at 70 °C for 10 min to obtain $MAPb(Br_{1-x}Cl_x)_3$ films. Subsequently, the PTAA solution was spin-coated on the perovskite film at 3000 rpm for 30 s. Finally, a 70 nm thick gold electrode was deposited by thermal evaporation. Devices after wire bonding were packaged by PDMS with two strategies. One is that we immersed devices into PDMS, the other is that we dropped the PDMS onto devices. These devices with PDMS were heated on hot plate at 60 °C for 1 h, and then kept in dry box for 12 h.

4.4. Characterization and measurements

To characterize the sample morphologies, field-emission scanning electron microscopy (JSM-7100F, JEOL) and focus ion beam (Helios G4 UX DualBeam FIB/SEM, FEI) were deployed. Ultraviolet-visible (UV–vis) absorption spectra were recorded on a Lambda 950 spectrophotometer (PerkinElmer) at room temperature. Steady-state PL measurements were carried out on an Edinburgh FS5 fluorescence spectrometer. The photoelectron spectroscopy in the air (PESA) was performed with the AC-2 PESA instrument (AC-2, RKI Instruments), combining an open counter with a UV source to position the valence band. X-ray diffraction (XRD) patterns were obtained by employing a PANalytical X-ray Diffractometer (X′pert Pro). The X-ray photoelectron spectra (XPS) were tested on the PHI 5000 Versaprobe III spectrometer (ULVAC-PHI). The current-time curves and current-voltage curves of devices were measured by Keithley 2450 source-meter, and a monochromatic xenon lamp source with tunable light intensity was used as a light source. The light intensity was calibrated with an optical power meter (Thorlabs, PM100D). An additional chopper was utilized to chop light into square wave optical signals with different frequencies. The active area for UV PD is 0.03 cm^2. Flexible UV PD was stuck on flat substrate to conduct the measurement after bent for different cycles. All the optoelectronic measurements were performed in ambient environment (at ~23–28 °C and ~45–55% relative humidity).

4.5. Wearable UV monitoring system

As schematically illustrated in Fig. S9a, ESP32-C3 (Espressif) microcontroller was used for signal acquirement, conditioning, and processing by its built-in 12 bit analog-to-digital converter (ADC), which also supported Bluetooth 5 (LE, Espressif) wireless communication with

tiny surface mounted ceramic antenna. The transimpedance amplifier and 2nd order low pass filter with 10 Hz cut-off frequency, which were built with high precision and low power consumption operational amplifier OPA376 (Texas Instruments), were applied to convert and preprocess analog signal from flexible UV PD. Commercial sensor HDC1080 (Texas Instruments) was employed for temperature and humidity monitoring. A 4.2 V 300mAh rechargeable lithium-ion polymer battery was used as a power supply. UV intensity was evaluated with UV index, which was classified into five levels with different color coding according to *Global Solar UV Index: A Practical Guide* published by World Health Organization. To visualize real-time UV index, a mobile Android Application was developed with Qt for Android platform, through which UV exposure could be recorded and further uploaded to cloud servers.

CRediT authorship contribution statement

Yu Zhou: Conceptualization, Methodology, Formal analysis, Investigation, Writing – original draft, Writing – review & editing; **Xiao Qiu:** Methodology, Formal analysis, Investigation, Visualization; **Zhu'an Wan:** Software, Validation, Data curation; **Zhenghao Long:** Validation, Writing – review & editing; **Swapnadeep Poddar:** Writing – review & editing; **Qianpeng Zhang:** Conceptualization; **Yucheng Ding:** Investigation; **Chak Lam Jonathan Chan:** Software; **Daquan Zhang:** Investigation; **Kemeng Zhou:** Resources; **Yuanjing Lin:** Resources; **Zhiyong Fan:** Supervision, Writing – review & editing; Project administration, Funding acquisition.

Declaration of Competing Interest

The authors declare that they have no known competing financial interests or personal relationships that could have appeared to influence the work reported in this paper.

Acknowledgements

Appendix A. Supporting information

Supplementary data associated with this article can be found in the online version at doi:10.1016/j.nanoen.2022.107516.

References

[1] J.S. Adams, T.L. Clemens, J.A. Parrish, M.F. Holick, N. Engl. J. Med. 306 (1982) 722–725.

[2] A.R. Young, K.A. Morgan, G.I. Harrison, K.P. Lawrence, B. Petersen, H.C. Wulf, P. A. Philipsen, Proc. Natl. Acad. Sci. 118 (2021) e2015867118.

[3] L. Rittié, G.J. Fisher, Ageing Res. Rev. 1 (2002) 705–720.

[4] F.R. de Gruijl, Eur. J. Cancer 35 (1999) 2003–2009.

[5] J. Moan, M. Grigalavicius, Z. Baturaite, A. Dahlback, A. Juzeniene, Photodermatol., Photoimmunol. Photomed. 31 (2015) 26–35.

[6] T.S.C. Foundation ⟨https://www.skincancer.org/skin-cancer-information/skin-cancer-facts/⟩, Accessed: 4, 2022.

[7] O. Polat Emre, G. Mercier, I. Nikitskiy, E. Puma, T. Galan, S. Gupta, M. Montagut, J. Piqueras Juan, M. Bouwens, T. Durduran, G. Konstantatos, S. Goossens, F. Koppens, Sci. Adv. 5 (2019) eaaw7846.

[8] N. Kollias, E. Ruvolo Jr., R.M. Sayre, Photochem. Photobio. 87 (2011) 1474–1475.
[9] D.L. Narayanan, R.N. Saladi, J.L. Fox, Int. J. Dermatol. 49 (2010) 978–986.
[10] Q. Yan, L. Gao, J. Tang, H. Liu, J. Semicond. 40 (2019), 111604.
[11] X. Huang, A.N. Chalmers, Ann. Biomed. Eng. 49 (2021) 964–978.
[12] M.E. Lee, A.M. Armani, ACS Sens. 1 (2016) 1251–1255.
[13] Y. Shi, M. Manco, D. Moyal, G. Huppert, H. Araki, A. Banks, H. Joshi, R. McKenzie, A. Seewald, G. Griffin, E. Sen-Gupta, D. Wright, P. Bastien, F. Valceschini, S. Seité, J.A. Wright, R. Ghaffari, J. Rogers, G. Balooch, R.M. Pielak, PLoS One 13 (2018), e0190233.
[14] M. Hou, H. So, A.J. Suria, A.S. Yalamarthy, D.G. Senesky, IEEE Electron Device Lett. 38 (2017) 56–59.
[15] J. Sun, S. Zhang, T. Zhan, Z. Liu, J. Wang, X. Yi, J. Li, P.M. Sarro, G. Zhang, J. Mater. Chem. C 8 (2020) 5409–5416.
[16] Y. Huang, L. Zhang, J. Wang, X. Chu, D. Zhang, X. Zhao, X. Li, L. Xin, Y. Zhao, F. Zhao, J. Alloy. Compd. 802 (2019) 70–75.
[17] A. Aldalbahi, E. Li, M. Rivera, R. Velazquez, T. Altalhi, X. Peng, P.X. Feng, Sci. Rep. 6 (2016) 23457.
[18] L.-X. Qian, Z.-H. Wu, Y.-Y. Zhang, P.T. Lai, X.-Z. Liu, Y.-R. Li, ACS Photonics 4 (2017) 2203–2211.
[19] X. Pan, T. Zhang, Q. Lu, W. Wang, Z. Ye, RSC Adv. 9 (2019) 37201–37206.
[20] X. Xu, J. Chen, S. Cai, Z. Long, Y. Zhang, L. Su, S. He, C. Tang, P. Liu, H. Peng, X. Fang, Adv. Mater. 30 (2018), 1803165.
[21] X. Liu, L. Gu, Q. Zhang, J. Wu, Y. Long, Z. Fan, Nat. Commun. 5 (2014) 4007.
[22] M.A. Green, A. Ho-Baillie, H.J. Snaith, Nat. Photonics 8 (2014) 506–514.
[23] L. Dou, Y. Yang, J. You, Z. Hong, W.-H. Chang, G. Li, Y. Yang, Nat. Commun. 5 (2014) 5404.
[24] S.D. Stranks, H.J. Snaith, Nat. Nanotechnol. 10 (2015) 391–402.
[25] Y. Zhang, S. Poddar, H. Huang, L. Gu, Q. Zhang, Y. Zhou, S. Yan, S. Zhang, Z. Song, B. Huang, G. Shen, Z. Fan, Sci. Adv. 7 (2021) eabg3788.
[26] G. Tang, F. Yan, J. Semicond. 42 (2021), 101606.
[27] S. Yip, L. Shen, J.C. Ho, J. Semicond. 40 (2019), 111602.
[28] X. Hu, X. Zhang, L. Liang, J. Bao, S. Li, W. Yang, Y. Xie, Adv. Funct. Mater. 24 (2014) 7373–7380.
[29] M.I. Saidaminov, V. Adinolfi, R. Comin, A.L. Abdelhady, W. Peng, I. Dursun, M. Yuan, S. Hoogland, E.H. Sargent, O.M. Bakr, Nat. Commun. 6 (2015) 8724.
[30] S. Tao, I. Schmidt, G. Brocks, J. Jiang, I. Tranca, K. Meerholz, S. Olthof, Nat. Commun. 10 (2019) 2560.
[31] Z. Chen, C. Li, A.A. Zhumekenov, X. Zheng, C. Yang, H. Yang, Y. He, B. Turedi, O. F. Mohammed, L. Shen, O.M. Bakr, Adv. Opt. Mater. 7 (2019), 1900506.
[32] W. Qarony, M. Kozawa, H.A. Khan, M.I. Hossain, A. Salleo, Y.H. Tsang, J. Y. Hardeberg, H. Fujiwara, D. Knipp, Adv. Mater. Interfaces 7 (2020), 2000459.
[33] G. Maculan, A.D. Sheikh, A.L. Abdelhady, M.I. Saidaminov, M.A. Haque, B. Murali, E. Alarousu, O.F. Mohammed, T. Wu, O.M. Bakr, J. Phys. Chem. Lett. 6 (2015) 3781–3786.
[34] T. Haeger, R. Heiderhoff, T. Riedl, J. Mater. Chem. C 8 (2020) 14289–14311.
[35] D. Liu, C. Yang, R.R. Lunt, Joule 2 (2018) 1827–1837.
[36] D. Solis-Ibarra, I.C. Smith, H.I. Karunadasa, Chem. Sci. 6 (2015) 4054–4059.
[37] Y. Liu, J. Wang, F. Wang, Z. Cheng, Y. Fang, Q. Chang, J. Zhu, L. Wang, J. Wang, W. Huang, T. Qin, Nat. Commun. 12 (2021) 3360.
[38] S.-F. Leung, K.-T. Ho, P.-K. Kung, V.K.S. Hsiao, H.N. Alshareef, Z.L. Wang, J.-H. He, Adv. Mater. 30 (2018), 1704611.
[39] T.M.H. Nguyen, S.K. Lee, S. Kim, C.W. Bark, ACS Appl. Mater. Interfaces 13 (2021) 57609–57618.
[40] K. Poorkazem, D. Liu, T.L. Kelly, J. Mater. Chem. A 3 (2015) 9241–9248.
[41] X. Hu, Z. Huang, X. Zhou, P. Li, Y. Wang, Z. Huang, M. Su, W. Ren, F. Li, M. Li, Y. Chen, Y. Song, Adv. Mater. 29 (2017), 1703236.
[42] L. Yu, L. Mao, Y. Li, X. Li, J. Zhang, Opt. Express 29 (2021) 7833–7843.
[43] H.S. Jung, K. Eun, Y.T. Kim, E.K. Lee, S.-H. Choa, Microsyst. Technol. 23 (2017) 1961–1970.
[44] Y. Jiang, L. Qiu, E.J. Juarez-Perez, L.K. Ono, Z. Hu, Z. Liu, Z. Wu, L. Meng, Q. Wang, Y. Qi, Nat. Energy 4 (2019) 585–593.
[45] X. Li, F. Zhang, H. He, J.J. Berry, K. Zhu, T. Xu, Nature 578 (2020) 555–558.
[46] S. Chen, Y. Deng, X. Xiao, S. Xu, P.N. Rudd, J. Huang, Nat. Sustain. 4 (2021) 636–643.

Yu Zhou received his B.E. and Ph.D. degree in Materials Science and Engineering from Tsinghua University, China in 2015 and 2020, respectively. Currently, he is a postdoctoral researcher working with Prof. Zhiyong Fan at The Hong Kong University of Science and Technology. His current research interests mainly focus on perovskite optoelectronics based on micro-nano structures.

Xiao Qiu is currently pursuing the Ph.D. degree in the Department of Electronic and Computer Engineering at The Hong Kong University of Science and Technology. He received his B.Eng. degree in New Energy Materials and Devices from Hefei University of Technology in 2020. His recent research focuses on nano-optoelectronic materials and devices.

Zhu'an Wan received his B.E. degree in Optoelectronic Information Science and Engineering from Huazhong University of Science and Technology, China in 2020. Currently, he is a Ph.D. student supervised by Prof. Zhiyong Fan at The Hong Kong University of Science and Technology. His current research focuses on semiconductor gas sensors and smart wearable devices.

Zhiyong Fan is currently a full professor at the Department of Electronic and Computer Engineering, The Hong Kong University of Science and Technology. He is a fellow of Royal Society of Chemistry and a founding member of The Hong Kong Young Academy of Sciences. His research interests are on the design and fabrication of novel nanostructures and nanomaterials for high-performance optoelectronics, energy harvesting devices, and sensors.